BIOPHYSICS LETTER

Fabien Nadrigny · Isabelle Rivals · Petra G. Hirrlinger
Annette Koulakoff · Léon Personnaz
Marine Vernet · Myriam Allioux · Myriam Chaumeil
Nicole Ropert · Christian Giaume · Frank Kirchhoff
Martin Oheim

Detecting fluorescent protein expression and co-localisation on single secretory vesicles with linear spectral unmixing

Abstract Many questions in cell biology and biophysics involve the quantitation of co-localisation and the interaction of proteins tagged with different fluorophores. However, the incomplete separation of the different colour channels due to the presence of autofluorescence, along with cross-excitation and emission "bleed-through" of one colour channel into the other, all combine to render the interpretation of multi-band images ambiguous. Here we introduce a new live-cell epifluorescence spectral imaging and linear unmixing technique for classifying resolution-limited point objects containing multiple fluorophores. We demonstrate the performance of our technique by detecting, at the single-vesicle level, the co-expression of the vesicle-associated membrane protein, VAMP-2 (also called synaptobrevin-2), linked to either enhanced green fluorescent protein (EGFP) or citrine (a less pH-sensitive variant of enhanced yellow fluorescent protein (EYFP)), in mouse cortical astrocytes. In contrast, the co-expression of VAMP-2-citrine and the lysosomal transporter sialine fused to EGFP resulted in little overlap. Spectral imaging and linear unmixing permit us to fingerprint the expression of spectrally overlapping fluorescent proteins on single secretory organelles in the presence of a spectrally broad autofluorescence. Our technique provides a robust alternative to error-prone dual- or triple colour co-localisation studies.

Keywords Spectral imaging · Linear unmixing · Fluorescence microscopy · Total internal reflection · Exocytosis · Protein expression · Co-localisation

F. Nadrigny · M. Vernet · M. Allioux · M. Chaumeil
N. Ropert · M. Oheim (✉)
Molecular and Cellular Biophysics of Synaptic Transmission,
Laboratory of Neurophysiology and New Microscopies,
INSERM U603, CNRS FRE 2500, Université René Descartes
(Paris 5), 45 rue des Saints Pères, 75 006, Paris, France
E-mail: fabien.nadrigny@univ-paris5.fr
E-mail: nicole.ropert@univ-paris5.fr
E-mail: martin.oheim@univ-paris5.fr
Tel.: +33-1-42864221
Fax: +33-1-42864151

I. Rivals · L. Personnaz
Applied Statistics Group, Ecole Supérieure de Physique et Chimie
Industrielles (ESPCI), 10, rue Vauquelin, 75 005, Paris, France
E-mail: isabelle.rivals@espci.fr
E-mail: leon.personnaz@espci.fr

P. G. Hirrlinger · F. Kirchhoff
Department of Neurogenetics, Max-Planck Institute
for Experimental Medicine, Hermann-Rein Strasse 3,
37 075, Göttingen, Germany
E-mail: petra.hirrlinger@em.mpg.de
E-mail: kirchhoff@em.mpg.de

A. Koulakoff · C. Giaume
Laboratoire deNeuropharmacologie INSERM U587,
Collège de France, 11, place Marcelin Berthelot,
75 005, Paris, France
E-mail: annette.koulakoff@college-de-france.fr
E-mail: christian.giaume@college-de-france.fr

Abbreviations CMV: Cytomegalovirus · CCCP: Carbonyl cyanide m-chlorophenylhydrazone · EYFP: Enhanced yellow fluorescent protein · FRET: Fluorescence resonance energy transfer · EDTA: Ethylenediaminetetraacetic acid · DMEM: Dulbecco's modified Eagle's medium · EF: Evanescent field · EGFP: Enhanced green fluorescent protein · FCS: Fetal calf serum · FP: Fluorescent protein · FWHM: Full-width half maximum · GFAP: Glial fibrillary acidic protein · P0–1: Postnatal days 0–1 · PBS: Phosphate-buffered saline · PS-CFP2: Photoswitchable cyan FP · SD: Standard deviation · ci: Confidence interval · SILU: Spectral imaging and linear unmixing · TIRF: Total internal reflection fluorescence · VAMP: Vesicle-associated membrane protein

Introduction

Classification and feature extraction methods based on multi- and hyperspectral imaging detectors are routine in remote sensing and satellite imaging (Chang 2003; Nielsen 2001). Applied to fluorescence microscopy (Dickinson et al. 2001; Hiraoka et al. 2002; Neher and Neher 2004a; Schultz et al. 2001; Shirakawa and Miyazaki 2004; Zimmermann et al. 2003, 2005), spectral imaging and linear unmixing (SILU) improves fluorescence resonance energy transfer (FRET) detection (Ecker et al. 2004; Gu et al. 2004; Neher and Neher 2004b) as well as the discrimination of fluorophores with spectral overlap that otherwise would not be resolved by dual- or triple band recordings (Lansford et al. 2001; Shirakawa and Miyazaki 2004; Tsurui et al. 2000).

The purpose of this study was to evaluate the performance of SILU for profiling the expression and co-localisation of fluorophores on resolution-limited point objects, which only emit a limited number of photons before photobleaching. This situation is typical for an increasing number of multi-colour cell biological, bioanalytical and biophysical applications that detect single-molecule FRET (Ishii et al. 1999), concentration microdomains (Demuro and Parker 2004), semiconductor nanocrystals (Grecco et al. 2004; Michalet et al. 2001), spectrally karyotype chromosomes (Garini et al. 1999) or image doubly labelled organelles in live cells (Ellenberg and Lippincott-Schwartz 1999; Stephens et al. 2000). A similar situation is encountered in double and multi-labelling experiments based on spectral variants of the green fluorescent protein (GFP) (Ellenberg and Lippincott-Schwartz 1999). Thus, although a wider colour range of fluorescent probes is becoming available, the choice of spectrally well-separated variants is still very restricted. For example, a recent study (Hirrlinger et al. 2005) demonstrated that the formation of fluorescent precipitates limits the use of red-emitting reef coral proteins in transgenic animals. Those FP that work best have considerable spectral overlap and cannot be separated using specific filter sets (Zimmermann 2005). Also, even if we were able to image two spectrally well-separated FP proteins, protein expression would still be obscured in many preparations by the presence of autofluorescence. Hence, although in a typical experiment the number of fluorophores is often limited to two or three, these may be strongly overlapping and therefore require unmixing.

Diffraction-limited imaging of point objects would benefit from our ability to record the spectral signature. An additional requirement when imaging, e.g. small organelles is to make efficient use of the few photons emitted before irreversible photobleaching. Therefore, rather than dividing the already low signal into several discrete non-overlapping colour channels, we optimised the fluorescence-collected fraction per excitation photon by "oversampling" (Garini et al. 1999) with few and wide channels with partially overlapping bands in sequential acquisitions (Zimmermann 2005).

Spectral unmixing is a *pixel-based* technique that quantifies the presence of several fluorophores in mixed pixels. It assigns a mixed pixel the fluorescence the pixel would have had if it consisted of a pure spectral component only. Due to their simplicity, linear models have gained significant popularity over mixing models with higher order moments (Bosdogianni and Petrou 1997) and are now available with commercial microscope software. The spectrum of each pixel is considered a linear superposition of the pure spectra present in that pixel, weighted by their relative fractional abundance, which is calculated by a least-squares estimation.

However, adjacent pixels on diffraction-limited images contain spatially and spectrally correlated information and cannot be considered independent. Further, due to the detector pixel size diffraction-limited point objects may only contain a handful of pixels so that the calculation of statistical descriptors may not be particularly reliable (Bosdogianni et al. 1997). We therefore investigated how the microscopic spatial resolution affects our ability to detect protein expression on single near-membrane astroglial vesicles identified on evanescent-field (EF) images. Robust statistics was ascertained, in a first step, by searching for and rejecting pixel outliers and then binning correlated pixels of Airy disk-sized regions centred on the single-vesicle images to extract noise-reduced organelle spectra. A reference spectral library contained average experiment spectra of the pure spectral components measured in live cells after cytoplasmic transfection. We verified that these spectra were not altered by the lower pH in secretory organelles (Kneen et al. 1998). The performance of SILU for single-vesicle classification was investigated in two realistic scenarios: (1) the co-localisation on the same organelle of a green and yellow FP and (2) their mutual exclusion by targeting citrine and EGFP to secretory vesicles and lysosomes, respectively. We also derived a statistical expression for quantifying the precision of the SILU-based fluorophore abundance estimates and investigated the relationship between the obtained precision and the signal-to-background ratio of the spectral images.

At the single-vesicle level, SILU permits us to fingerprint the expression and co-localisation of spectrally overlapping fluorescent proteins on individual near-membrane organelles.

Theory and qualitative concept

In this work, a "mixed pixel" is defined as the two-dimensional (2D) representation on the imaging detector of the corresponding 3D sample volume ("voxel") that contains one or several fluorophores with non-zero probability. The emission of a mixed pixel is alternately viewed through five band-pass filters upon single-wavelength epifluorescence excitation. In a mixed pixel, some non-zero fraction of the collected signal arises from endogenous fluorophores (cellular autofluorescence) and from the exogenous fluorescent labels, each of which

imprint their spectral signature on the recorded emission spectrum. We consider here the example of mouse cortical astrocytes, cells known to express appreciable levels of autofluorescence (Anlauf and Derouiche 2005; Schipper et al. 2002), labelled with a mixture of EGFP and citrine (Griesbeck et al. 2001). Due to bleed-through and spectral overlap each channel does not represent a single species. However, the five-point spectrum is unique for each of the pure species ("endmembers" in the remote sensing terminology), i.e. any mixed pixel is a linear combination of the pure spectral components. If these spectral unit vectors are experimentally predetermined in three specially prepared samples in which only one pure species is present (or dominating), then the contribution of EGFP, citrine and autofluorescence present in any unknown pixel can be calculated based on the intensities they produce in the spectral bands.

In our experimental system, there are three unknown contributions: autofluorescence, EGFP and citrine. Therefore, at least three independent measurements are needed to find a unique solution for all three contributions. To be less sensitive to image noise and to better distinguish yellow-green fluorescent probes, we slightly oversampled the yellow-green part of the spectrum by detecting three yellow-green spectral bands and one orange and red band, respectively. Although all the necessary information is contained in these coarse spectra, three important practical questions are raised: (1) How much variability in the fluorophore spectra can be tolerated to reliably distinguish spectrally close fluorophores? (2) How sensitive are the results to spectral variability (e.g. due to multiple molecular fluorophores that contribute to the compound autofluorescence spectrum) or to pH-dependent changes of the fluorophore spectra? and (3) How robust is the SILU technique for analysing very dim point objects? These questions are addressed here theoretically and experimentally.

Materials and methods

Cells, labelling and solutions

Primary astrocyte cultures were prepared as described (Rouach et al. 2003). Briefly, cortices from newborn (P0–1) OF-1 mice were dissected in PBS/glucose, meninges peeled off and the tissue mechanically dissociated. Cells were seeded in tissue culture flasks supplemented with 10% FCS, 10 U/ml penicillin and 10 µg/ml streptomycin. After reaching confluence they were harvested with trypsin–EDTA, plated as secondary cultures on 25 mm coverslips (Superior, Marienfeld#1, Lauda-Königshofen, Germany) and used 6–11 days after preparation. We identified astrocytes by their morphology, immunocytochemical staining with antibodies against glial fibrillary acidic protein (>96% were GFAP-positive) and by the presence of mechanically evoked spreading $[Ca^{2+}]$ waves (not shown). For recordings, coverslips were transferred to a holder on the microscope stage and perfused at 1–2 ml/min with extracellular solution containing, in mM: 140 NaCl, 5.5 KCl, 1.8 CaCl$_2$, 1 MgCl$_2$, 20 glucose, 10 HEPES (pH 7.3). All experiments were carried out at 20–22°C.

Plasmids and transfections

To highlight astroglial secretory and lysosomal compartments, respectively, we transfected $\sim 10^5$ cells per coverslip with 2 µg/ml synaptobrevin-2-citrine fusion protein (Griesbeck et al. 2001) under the control of the cytomegalovirus (CMV-)promoter (Fig. 1a, pCMV-sb2-citrine-N1, Wojcik et al. 2004, a gift from Dr. Sonja Wojcik, Göttingen, Germany), pCMV-sb2-EGFP-N1 (a gift from Dr. Jean-Pierre Mothet, Gif-sur-Yvette, France) or pCMV-EGFP-sialine-N1 (Morin et al. 2004) (Fig. 1b, a gift from Dr. Bruno Gasnier, Paris, France) using lipofectamin 2000 (Invitrogen, Carlsbad, CA, USA) and standard protocols. For double transfections, we maintained the same amount of DNA, which we equally divided between pCMV-EGFP-sialine-N1 and pCMV-sb2-citrine-N1. Transfected cells were incubated overnight and imaged on the following day. Control transfections with cytoplasmically expressed fluorescent proteins only (e.g. pEGFP-N1, Clontech, BD Biosciences, Franklin Lakes, NJ, USA) ascertained the specific targeting of protein constructs (Fig. 1a, b, insets).

Evaluating the effect of pH changes on experimental reference spectra

To evaluate the effect of fluorescent protein exposure to cytoplasmic (7.3) versus vesicular pH (5–5.5), we recorded EGFP and citrine reference spectra in control conditions and in acidified cells using a protocol similar to Kneen et al. (1998). Cortical astrocytes were transfected with pEGFP-N1 and pCitrine-N1 as above. After initial incubation in standard extracellular saline, the medium was replaced by a series of calibration solutions containing the same salt concentrations and additionally the protonophore CCCP (20 µM) and K^+/H^+ exchanger nigericin (10 µM). The pH values were sequentially adjusted to 7.3 (control), 5.4, 5.2, 5.0, 4.8 and 4.3. We monitored the evolution of 488/535 nm fluorescence every 3 min. Equilibration was reached after 10 min and the spectrum for each pH value was recorded thereafter from small cytoplasmic regions. To ascertain that the variation in fluorescence intensity and spectrum was indeed due to pH changes, we confirmed the fluorescence recovery by reversal to pH 7.3 (data not shown). Although citrine is less pH-sensitive than EYFP a slight spectral shift was observed (see Fig. 3b) below pH 5.0, which is not believed to interfere with our SILU imaging of secretory vesicles (pH 5–5.5), see Discussion.
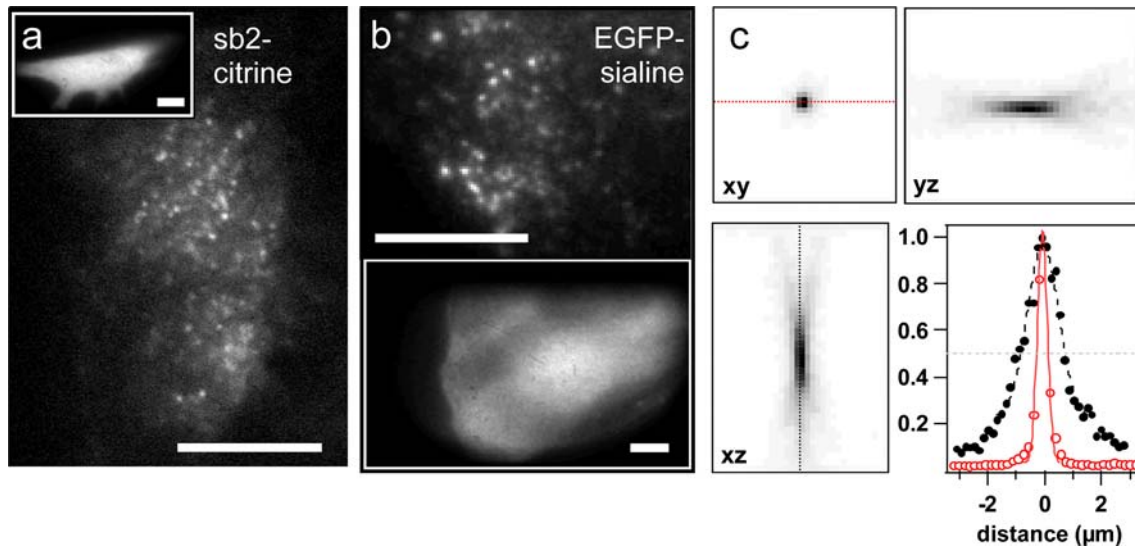
Fig. 1 a Evanescent-field imaging of near-diffraction-limited astroglial vesicular compartments. Raw data 514/560 nm evanescent-field (EF) excited fluorescence image of a synaptobrevin (sb2)-2-citrine transfected astrocyte and cytoplasmic control transfection with citrine alone (*inset*). Note the partial targeting of sb2 to the plasma membrane, seen as a fluorescent haze upon EF excitation. **b** Raw data 488/535 nm EF image of a EGFP-sialine-transfected astrocyte and control (*inset*). *Scale bars* are 10 μm for **a** and **b**. **c** Examples of 488/535 nm in focus *xy* epifluorescence image and *xz*- and *yz*-projection images of a 93 nm fluorescent bead (Invitrogen) and normalised fluorescence intensity line profiles. Pixel size 188 nm, distance between planes 158 nm. Contrast is inverted for clarity. The experimental point-spread function had a lateral and axial FWHM of 308 ± 1 nm (*red*) and 2.19 ± 0.16 μm (*black*), respectively. We calculated 342 ± 1 nm ($n = 27$ beads) as the radius of the Airy disk from the first minimum of a Bessel function with the same FWHM. Compound magnification was ×120, numerical aperture (NA) 1.45
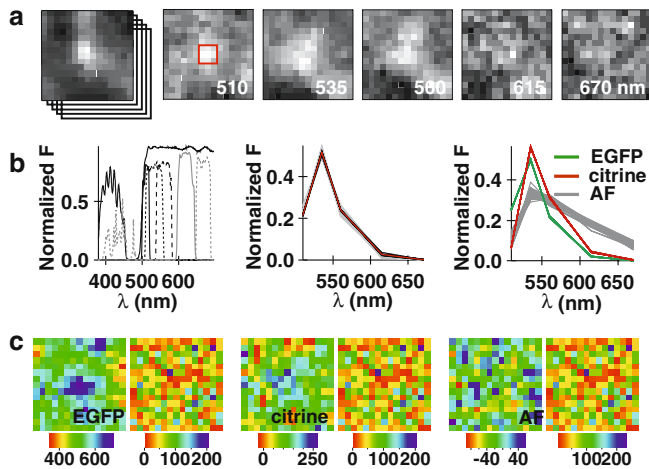

Fig. 2 a Total internal reflection fluorescence (TIRF) image of a sb-2-EGFP and sb2-citrine co-labelled astroglial vesicle (×120, NA-1.45) and spectral 510-535-560-615-670 nm epifluorescence image cube. *Scale bar* is 1 μm. **b** *Left* Filter spectra. *Middle* 81 mixed pixels (*grey* traces) contain the composite spectrum of the fluorophores present in the corresponding sample voxel. Binning the nine organelle pixels (*black* traces) to an Airy disk-sized region (*red* on *a*) reduces the pixel-to-pixel spectral variability and yields a noise-reduced spectrum (*red* trace). Pure FP spectra (*right*) were measured in the cytoplasm of cells transfected with EGFP or -citrine alone, and, for autofluorescence (AF), in unlabelled cells, respectively. **c** Unmixed reconstituted fluorophore abundance maps showing the participation to the vesicle shown on *a* of EGFP, citrine and AF and their 70% confidence interval of the estimate, respectively. Error images are almost alike due to equal-energy normalisation (see Materials and methods). Note the different intensity scales for the reconstituted images. (A colour version of this figure is available online)

Multispectral single secretory organelle imaging

We imaged cells on a custom-inverted microscope equipped for EF and epifluorescence excitation (see Schapper et al. 2003 for details). EF excitation was achieved by focusing the attenuated spectrally and spatially filtered 488-nm beam of a multi-line argon laser (Reliant 150, Laser Physics, West Jordan, UT, USA) into the back focal plane (BFP) of a ×60/NA-1.45 oil-immersion objective (PlanApochromat, Olympus, Hamburg, Germany). The location of the focal spot in the BFP determined the angle θ under which the collimated beam impinged on the surface of the microscope slide. For $\theta \geq \theta_c = \arcsin(n_2/n_1)$ the 488 nm beam suffers total internal reflection (TIR). $n_2 = 1.35$ and $n_1 = 1.518$ are the refractive indices of the cell and the substrate, respectively, so that $\theta_c = 62.8°$. We used a $\sim$200 nm penetration depth of the evanescent field, corresponding to $\theta = 66.2° \pm 0.1°$. A Polychrome II (TILL, Gräfelfing, Germany) provided narrowband ($\lambda \pm 8$ nm) polychromatic epifluorescence excitation.

We used a 500DCLP dichroic mirror (Chroma, Brattleboro, VT, USA) and discrete emission filters housed in a motorised and computer-controlled filter wheel [HQ510/20 (solid line on Fig. 2b, left panel), HQ535/50 (dashed), HQ560/40 (line-dashed), HQ615/45 (grey, solid), HQ670/40 (grey, dashed)] to acquire epifluorescence spectral image cubes. Gain and exposure times were identical for all planes. Over dividing the fluorescence emission into multiple colour channels, e.g. with a commercial 4-channel emission beam splitter, the

sequential acquisition maximises the number of useful signal photons per excitation photon, albeit at lower time resolution. In as much as we did not continuously acquire spectral image cubes but rather took a spectral "snapshot" to classify the viewed organelles at the beginning of a single-colour time-lapse acquisition, this approach is not detrimental to acquiring high-time resolution data (see Discussion). To verify that photobleaching did not deleteriously affect the sequentially collected emission spectra (Neher and Neher 2004a), we collected spectra in both ascending (510–670 nm) and descending orders. The emission profiles detected for the various fluorophores were identical (not shown). As a corollary, this observation equally illustrates the robustness of the SILU technique over time.

The resulting images were projected onto a GenIII-intensified PentaMax charge-coupled device (CCD) camera (Roper Scientific, Trenton, NJ, USA), generously provided by Dr. Maïté Coppey-Moissan (Institut Jacques Monod, Paris, France). A custom telescope matched the camera pixel size to the calculated resolution. We acquired spectral image cubes with 1 s time resolution, which was sufficient to track moving organelles visually on consecutive frames, using METAMORPH software (Universal Imaging, Downington, PA, USA).
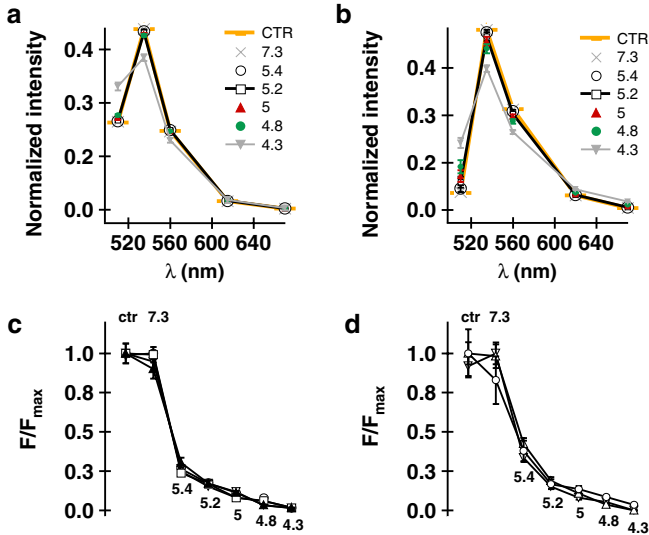

Fig. 3 a The spectrum of cytoplasmically expressed EGFP is pH invariant down to pH 4.8. For citrine (b), no appreciable variation is detected down to pH 5.2. To ascertain that the pH in the cytoplasm actually changes despite the absence of a detectable spectral change, we monitored the fluorescence intensity. For EGFP (c) as for citrine (d), we observe a pronounced decrease of the fluorescence intensity between pH 7.3 and 5.4, as expected from their respective pKa values (5.9 and 5.7 for EGFP and citrine, respectively). Plots show averages and SD of the fluorescence recorded from five ROIs in three groups of cells for EGFP and three ROIs from two groups of cells for citrine. *CTR* is the value measured before permeabilisation. Note the larger relative error on citrine and compare to EGFP traces. (A colour version of this figure is available online)

Extracting mixed organelle spectra

We subtracted from the raw spectra background spectra taken with the same gain and exposure time in cell-free regions close to the studied organelle. To compensate the lateral offset resulting from different filter thickness and organelle movement we excised from the full images $3{\times}3\ \mu m^2$ regions of interest (ROIs) centred on the individual fluorescent spot. No systematic criteria were applied concerning the signal-to-background ratio (SBR; see, however, Fig. 6), but organelles were rejected when their lateral full-width half maximal (FWHM) size exceeded 1.5× the Airy disk so that only near-diffraction-limited spherical spots were conserved (Fig. 1c). For spectral analysis, normalized fluorophore spectra to equal energy, $\mathbf{w}^*(i) = \mathbf{w}(i)\Big/\left(\sum_{k=1}^{N} w_k(i)\right), \forall i.$ As we shall operate with normalised quantities only the asterisk is omitted. We read out nine single-pixel spectra from the 3×3 central pixels (0.5×0.5 μm^2) encompassing the central maximum of the Airy disk. Due to the diffraction-limited resolution, these pixels contain spatially and spectrally related information and should be realisations of the same spectral vector only varying by additive noise. We therefore asked whether the spectral vector

$$\mathbf{w}(x,y) = (w_1(x,y), w_2(x,y), \ldots, w_N(x,y))^{\mathrm{T}} \qquad (1)$$

of pixel x, y belonged to the vector bundle spanned by the other eight vectors $\mathbf{w}(x',y')|_{(x',y')\neq(x,y)}$ by testing if $\mathbf{w}(x, y)$ was an outlier. Here, N denotes the number of channels. We tolerated two outlier pixels per organelle. This choice relates to the SBR in the experiment. Testing against outliers (null hypothesis) in dim images with too low SBR will falsely discard related but noisy pixel vectors. If a pixel (x, y) is not an outlier, then (Eq. 2)

$$\frac{P-2}{P}\left\|\mathbf{w}(x,y) - \overline{\mathbf{w}(x',y')}\right\|\Big/\sum_{k=1}^{N}\sigma_k^2(x',y') \qquad (2)$$

is a *Fisher* variable, $F_{(P-2)N}^{N}$. $\overline{\mathbf{w}(x',y')}$ is the average spectrum of the eight pixels exempt (x, y), $\sigma_k^2(x', y') = \frac{1}{P-1}\sum x', y'(w_k(x',y') - \overline{w_k(x',y')})^2$ and F is the "*F-*" or *Fisher–Snedecor* distribution[1] and $\|\quad\|$ denotes the vector norm. We accepted a 15% risk of falsely classifying $\mathbf{w}(x, y)$, $f_{85\%} = 1.75$, which is motivated by the detectable signal change limited by the shot noise contribution, $\sqrt{S}$, to the dim single-vesicle signal S and the amount of signal per grey value in the image (Oshiro and

---

[1]This result supposes that both the numerator and the denominator follow Pearson's law. We here assume that the noise is Gaussian. The anisotropic fluorescent environment aroudn the spot, the presence of readout and intensifer noise add uncorrelated noise to each pixel so that they are realisations of events with the same mathematical expectation value plus noise. As the N components of the spcetral vector $\mathbf{w}(x,y)$ are acquired successively, they are statistically independent and their quadratic sum in the numerator of Eq. 2 is described by Pearson's law. In the same way, the denominator is Pearson-distributed.

Moomaw 2003). We binned correlated pixels to extract a noise-reduced spectrum,

$$\mathbf{w}(i) = (w_1(i), w_2(i), \ldots, w_N(i))^\mathrm{T} \qquad (3)$$

(red trace on Fig. 2b, middle panel), where i is the index of the spot.

Linear unmixing

We used a non-constrained supervised ordinary least-squares linear unmixing (Nielsen 2001) of noise-reduced mixed organelle spectra. Specifically, we assumed that (1) endmembers are predefined pure classes with 100% fluorophore abundance. This implies, that we can measure pure fluorescent protein spectra by overexpressing one protein so that cellular autofluorescence becomes negligible. (2) All pure spectral components present are known. (3) In contrast to constrained algorithms (see, e.g. Zimmermann et al. 2003) the non-negativity of the abundance coefficients α_k was not imposed, and (4) the abundance coefficients were not forced to sum to unity, $\sum_{l=1}^{m} \alpha_l = 1$. As a consequence, solutions to the unmixing problem can be located outside physically meaningful regions of the parameter space (see, e.g. Fig. 4b). Hence, if the confidence interval of the estimation was smaller than the separation distance from the allowed region,

the analysed spot was rejected. (5) Also, we assumed that the signal of each fluorescent spot consists of a *linear* mixture of m pure spectral components, i.e. we neglected higher orders allowing for fluorophore interaction, saturation and quenching effects. Normalised spectral vectors $\mathbf{w}(i)$ were compared with a $N \times m$ reference spectral matrix,

$$\mathbf{X} = ((x))_{kl} = \begin{pmatrix} x_{11} & \cdots & x_{1m} \\ \vdots & \ddots & \vdots \\ x_{N1} & \cdots & x_{Nm} \end{pmatrix} = (\mathbf{x}_1 \quad \cdots \quad \mathbf{x}_m),$$

$$(4)$$

where $l \in [1, m]$ varies over pure spectral classes and $k \in [1, N]$ varies over wavelengths λ. (6) We did not include an additional constant column vector, i.e. we considered background subtraction to completely remove any transmitted light or amplifier offset.

Pure spectral vectors $\mathbf{x}_1$ (Fig. 2b, right) were measured averages, for autofluorescence, from unlabelled cells, for EGFP and citrine from autofluorescence-free cytoplasmic regions of astrocytes transfected with pEGFP-N1 (Clontech) or pCMV-citrine-N1, respectively (Fig. 1, insets). According to our mixing model the quantity of pure spectra in a mixed spot is a m-vector $\hat{\alpha}(i)$ such that
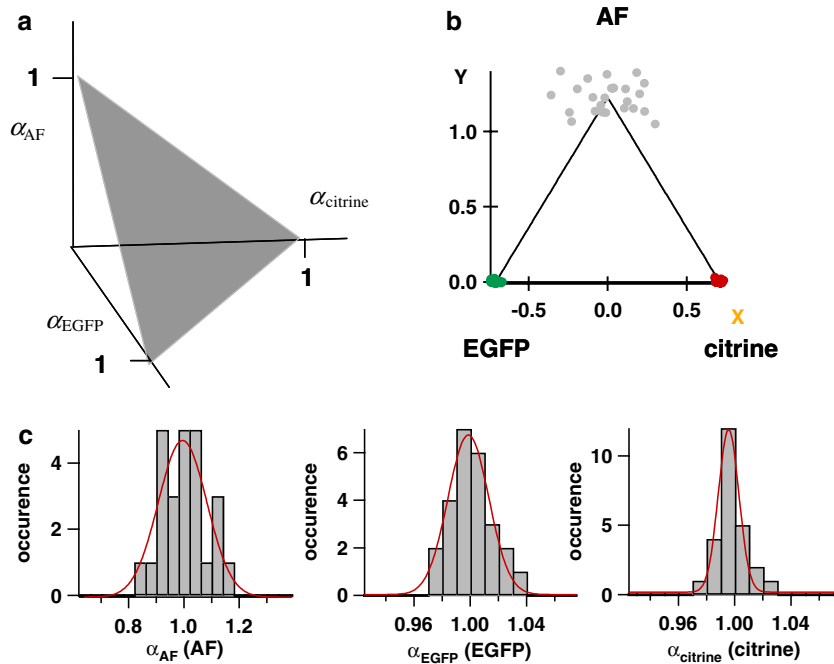

Fig. 4 a Estimated spectral abundances define vectors in a three-dimensional (3D) space spanned by the pure component unit vectors. **b** We parameterised (see Appendix) the plane shaded in **a** so as to represent the endpoints of vectors $\hat{\alpha}(i)$ on a 2D graph. *Green*, *red* and *grey* spots indicate projected spectral abundance vectors of EGFP $\hat{\alpha}$ (EGFP), citrine, $\hat{\alpha}$(citrine), and autofluorescence, $\hat{\alpha}$(AF), respectively. The larger spread observed for AF is due to the bigger variation of the spectra of autofluorescent regions. See also Table 1. **c** Distribution of the pure components α'_{EGFP} (EGFP) (*green*) and $\alpha'_{\mathrm{citrine}}$ (citrine) (*red*) for 25 unmixed control regions each containing either pure EGFP or citrine, and Gaussian fits (*red*), respectively. Their Gaussian distribution justifies the used statistical tools to determine the confidence interval of the fluorophore abundance estimate. (A colour version of this figure is available online)

$$\mathbf{w}(i) = \mathbf{X} \cdot \hat{\alpha}(i) + \mathbf{r}(i). \tag{5}$$

The components of $\hat{\alpha}(i) = (\alpha_{\mathrm{EGFP}}(i), \alpha_{\mathrm{citrine}}(i), \alpha_{\mathrm{AF}}(i))$ are the estimated fluorophore abundances, $\mathbf{r}(i)$ is the residual not explained by the linear mixing model. When the number of detection channels is larger than the number of spectral components, $N \geq m$, $\hat{\alpha}(i)$ is obtained by minimising the sum of the squared residuals $\mathbf{r}^{\mathrm{T}} \cdot \mathbf{r}$. For ordinary least squares, $\hat{\alpha}$ is non-biased, i.e. $E\{\hat{\alpha}\} = \alpha$ with dispersion $(\mathbf{X}^{\mathrm{T}} \cdot \Sigma_r^{-1} \cdot \mathbf{X})^{-1} = (\mathbf{X}^{\mathrm{T}} \cdot \sigma^2 \cdot \mathbf{X})^{-1}$ where σ^2 is the variance of the noise, so that $\hat{\alpha} = (\mathbf{X}^{\mathrm{T}} \mathbf{X})^{-1} \mathbf{X} \cdot \mathbf{w}$ with dispersion $\sigma^2 (\mathbf{X}^{\mathrm{T}} \mathbf{X})^{-1}$. By assuming that the noise is independent among the N channels with equal variance and is normally distributed with expectation value $E\{\mathbf{r}\} = 0$, see Fig. 4c, we can interpret the confidence region for α, by noting that

$$(\hat{\alpha} - \alpha)^{\mathrm{T}} \mathbf{X}^{\mathrm{T}} \cdot \mathbf{X}(\hat{\alpha} - \alpha) \cdot \frac{N - m}{m \cdot \mathbf{r}^{\mathrm{T}} \mathbf{r}} \rightarrow F_{N-m}^m. \tag{6}$$

We chose $\Delta \hat{\alpha} = \hat{\alpha} - \alpha$ to be 70% confidence level in analogy to an m-dimensional SD. The confidence region of alpha is an m-dimensional ellipsoid.

Detecting protein expression in a resolution-limited sample voxel

To detect fluorescent protein expression in a fluorescent spot i (irrespective of the fluorescent protein) we first tested if its normalised spectral vector $\mathbf{w}(i)$ statistically differed from the autofluorescence bundle $\{\mathbf{w}(\mathrm{AF})\}$,

$$\frac{L - 1}{L + 1} \cdot \left\| \mathbf{w}(i) - \overline{\mathbf{w}(\mathrm{AF})} \right\|^2 \bigg/ \sum_{k=1}^{N} \sigma_k^2(\mathrm{AF}) \rightarrow F_{N(L-1)}^N. \tag{7}$$

Here $\overline{\mathbf{w}(\mathrm{AF})} = (1/L) \sum_{j=1}^{L} \mathbf{w}(j)$ and $\sigma_k^2(\mathrm{AF}) = (1/L) \sum_{j=1}^{L} \left(\mathrm{w}_k(j) - \overline{\mathbf{w}(\mathrm{AF})} \right)^2$. $L = 25$ is the number of autofluorescent pure vectors of the AF vector bundle and j is their index. We tolerated a 5% false positive detection of protein presence ($t_{95\%} = 2.31$). Spectral unmixing permits the estimation of the fractional abundance of the fluorophores present in the studied object. To correct for different levels of autofluorescence within and among cells and to reduce the problem to two dimensions we re-expressed the 3D spectral abundance vector $\hat{\alpha}$ by a re-normalised 2D vector,

$$\hat{\alpha}' = (\alpha'_{\mathrm{EGFP}}, \alpha'_{\mathrm{citrine}}) = (\alpha_{\mathrm{EGFP}}, \alpha_{\mathrm{citrine}}) / (1 - \alpha_{\mathrm{AF}}), \tag{8}$$

that only contains the exogenous fluorophores. Normalising by $1 - \alpha_{\mathrm{AF}}$ instead of $\alpha_{\mathrm{EGFP}} + \alpha_{\mathrm{citrine}}$ allows to take into account the residual. Vectors $\hat{\alpha}'$ are conveniently represented on a parametric plot of α'_{EGFP} versus $\alpha'_{\mathrm{citrine}}$ (Fig. 5). Once the problem reduced to two dimensions, we searched for the presence in voxel i of EGFP and citrine, respectively, by comparing the measured $\hat{\alpha}'$ to the previously characterised pure bundles $\{\hat{\alpha}'\}_{\mathrm{EGFP}}$ and $\{\hat{\alpha}'\}_{\mathrm{citrine}}$. The expression

$$\frac{\alpha'_l(i) - \overline{\alpha'_l(\mathrm{EGFP})}}{\sqrt{\frac{1}{L} \sum_{j=1}^{L} \left(\alpha'_l(j) - \overline{\alpha'_l(\mathrm{EGFP})} \right)^2}} \cdot \sqrt{\frac{L - 1}{L + 1}}$$
$$\rightarrow \mathrm{Student}(L - 1), \tag{9}$$

if no fluorophore other than EGFP is present, and similar for citrine. Here, L is the number of ROIs j that defined the pure spectral vector bundle $\{\hat{\alpha}'\}_{\mathrm{EGFP}}$, $\alpha'_l(i)$ is the re-normalised spectral abundance of fluorophore l in voxel i, $\overline{\alpha'_l(\mathrm{EGFP})} = \frac{1}{L} \sum_{j=1}^{L} \alpha'_l(j)$ and the denominator in Eq. 9 is the SD of the $\alpha'_l(j)$ about their average $\overline{\alpha'_l(\mathrm{EGFP})}$. Student's test defines zones of fluorophore presence. Their 95% confidence intervals are shown on the parametric plots for binary mixtures ($m = 2$) as broken lines (Fig. 5). Thus, fluorophore presence can conveniently be read off graphically; an unmixed ROI within the rectangular region spanned by the broken lines contains both fluorophores.

Statistical significance between data sets was assessed by F-test and Student's t test, when applicable. Parameters are given in the text and figures. We defined the confidence interval of the estimated fluorescence abundance estimates to have the same statistical significance as an m-dimensional SD.

Results

Evanescent-field images of mouse cortical astrocytes transfected with constructs encoding a sb2-citrine fusion protein (Fig. 1a, pCMV-sb2-citrine-N1, Wojcik et al. 2004) or the lysosome-specific transporter sialine-EGFP (Fig. 1b, pCMV-sialine-EGFP-N1, Morin et al. 2004) revealed a dense pattern of punctate green fluorescence. To further characterise these diffraction-limited near-membrane spots, we acquired five spectral images in rapid succession and excised from the 510-535-560-615-670 nm epifluorescence image cube 3×3 $\mu\mathrm{m}^2$ ROIs) containing a single near-diffraction-limited spot. We used epifluorescence excitation instead of TIRF for the acquisition of spectral images because SILU is an intensity-based technique and thus sensitive to defocus and out-of-focus movement artefacts. Wide-field excitation epifluorescence samples a hour-glass-shaped volume that is fairly insensitive to submicrometre axial vesicle movement (see PSF in Fig. 1c), whereas the exponentially decaying evanescent field magnifies axial movements, resulting in biased fluorophore abundance estimates (data not shown). The use of epifluorescence excitation reduces the axial optical sectioning. Negligible out-of-focus contamination requires to chose fairly isolated spots which is facilitated by the low organelle density in astrocytes (see Discussion).

Roughly 30% of the spots seen in epifluorescence appeared on EF excited images and ~50% of the spots seen on EF images were also visible on the corresponding epifluorescence images. The latter finding is explained by the higher contrast offered by EF excited
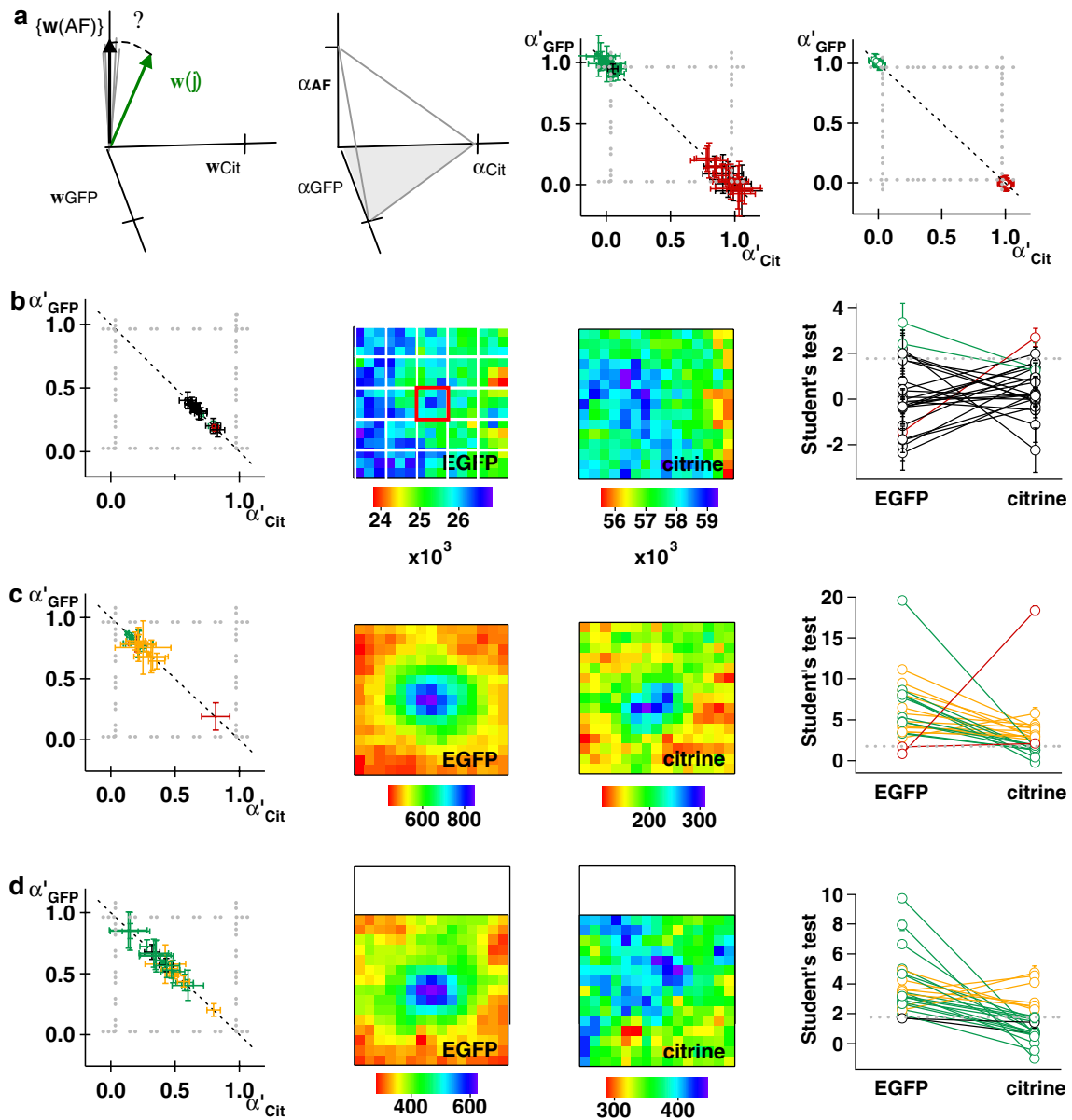
Fig. 5 Detecting vesicular protein expression and co-localisation. **a** *Left* Fluorescent protein (FP) expression was detected by testing if spectral vector **w**(*i*) was an outlier relative to the autofluorescence vector bundle {**w**(AF)}. *Middle left* To compare across organelles and cells with varying AF level, we re-normalised $\hat{\alpha} \rightarrow (\alpha'_{EGFP}, \alpha'_{citrine})$ that lie coplanar in the plane spanned by pure EGFP and citrine unit vectors (*shaded*). *Middle right* Astrocytes transfected with synaptobrevin-2 (sb2)-EGFP (*green*) or sb2-citrine (*red*) alone showed no co-localisation (see Table 2 for details). *Black crosses* indicate spots for which no decision was possible with the desired 95% confidence. *Right* Cytoplasmic expression of EGFP (*green*) or citrine (*red*) alone determined the detection threshold for the presence of both fluorophores (*dashed*). **b** Cytoplasmic co-transfection of EGFP and citrine is detected as co-expression. *Middle panels* Comparison on reconstituted images of FP presence in the central (*red square*) versus peripheral regions of interest (ROI) (testing for outliers, Student's test, 95% confidence, $t_{95\%}$) discards these false positives (*black symbols*). *Right* Each analysed spot is represented by a *barbell*. Endpoints report $t_{95\%}$ values for the presence of EGFP and citrine on the organelle if $t_{95\%} > 1.76$ (*dotted line*). *Red symbols* indicate ROIs that SILU classifies as citrine-positive organelles, *green* indicates EGFP expression, *black* are organelles below $t_{95\%}$. **c** Same type of analysis for 25 organelles in sb2-EGFP and sb2-citrine co-transfected astrocytes. A majority display both EGFP and citrine (*yellow*). On the reconstituted fluorophore abundance maps, a central maximum for both EGFP and citrine fluorescence is detected. See Table 2 for details. **d** When expressing citrine and EGFP on secretory vesicles (sb2-citrine) and lysosomes (by tagging the lysosome-specific transporter sialine with EGFP), respectively, about two-thirds of the organelles express EGFP only. This is explained by the observation that in cultured astrocytes lysosomal compartments outnumber secretory vesicles. About one quarter of lysosomes also contained citrine, probably indicating the uptake and degradation of membranous sb2-citrine. See Table 2 for details. *Middle images* show the example of an EGFP-positive and citrine-negative organelle. (A colour version of this figure is available online)

fluorescence that permits the visualisation of puncta that are drowned in a diffuse haze on epifluorescence images. Using combined EF detection and spectral epifluorescence imaging, we analysed a total of 250 single-spot images from the footprint regions of 45 mouse cortical astrocytes making close contact with the coverslip. Of these ROIs, 128 contained vesicles (or lysosomes), 122 were cytoplasmic control regions. We only analysed and unmixed spots that were detected on both evanescent-field and epifluorescence images.

SILU estimates of fluorophore abundance are susceptible to errors introduced to the raw images by spurious background due to inefficient filtering, the Poisson noise of the fluorescence signal itself and the detector readout noise. Also, by collecting a spectrum for each pixel, the multispectral image picks up the spectral properties of the corresponding sample voxel (Fig. 1c). Thus, when imaging fluorescent sub-resolution objects, adjacent pixels on the diffraction-limited image contain correlated information. We note that this situation is different from that encountered in remote sensing and satellite imaging applications, where mixed pixels arise from fine variations in soil coverage present in the single-pixel image. Such mixed pixels are independent and can (and should indeed) be unmixed individually. Since the precision of unmixing depends on the accuracy of the sample and reference spectra (Fig. 2b, right; see Neher and Neher 2004a for details), binning the nine pixels of an Airy disk-sized (0.5×0.5 μm^2) ROI centred on the organelle image for extracting the noise-reduced spectrum $\mathbf{w}(i)$ of organelle i is expected to increase the precision of fluorophore abundance estimates (red on Fig. 2). We ascertained the spectral homogeneity within the Airy disk by testing the pixel spectra for outliers (F-test, $t_{85\%} = 1.75$, see Materials and methods for details). The participation of a fluorophore to a mixed 0.5×0.5 μm^2 ROI centred on the single-spot image was estimated by solving $\mathbf{w}(i) = \mathbf{X}\hat{\alpha}(i) + \mathbf{r}(i)$ for $\hat{\alpha}(i)$ in the least-squares error sense. $\mathbf{X}$ is the $N \times m$ matrix of measured pure spectra $\mathbf{x}_l$ (Fig. 2b, right panel), $\hat{\alpha}(i)$ the vector estimating the fractional abundance of pure spectra and $\mathbf{r}(i)$ the residual not explained by the linear mixing model. As fully constrained SILU methods are known to be less effective than partially constrained techniques (Chang 2003), we used a supervised least-squares error minimisation unmixing without constraining α_l to be non-negative nor imposing a sum-to-one constraint (see Materials and methods for details).

A common interferer in biological imaging is autofluorescence (AF) that can obscure the emission of exogenous fluorophores (see Fig. 2b, right). Therefore, we first verified whether SILU recognised pure spectral components in unlabelled (autofluorescent) and mock-transfected cells that homogeneously expressed in their cytoplasm pCMV-EGFP-N1 or pCMV-citirine-N1, respectively (see Fig. 1a, b, *insets*). In the absence of image noise, SILU should reconstitute unitary abundance vectors $\hat{\alpha} = (\alpha_{EGFP}, \alpha_{citrine}, \alpha_{AF})$ with only one non-zero component in the dimension corresponding to the respective fluorophore.

One concern is that SILU relies on the precision of the reference spectra used. In order not to interfere with vesicle docking and fusion, sb2-EGFP, sb2-citrine and EGFP-sialine express the fluorophore on the lumenal rather than the extravesicular side so that the fluorophore is exposed to the acidic intravesicular environment. We therefore verified the influence of pH on the reference spectra and unmixing. In controls using permeabilised astrocytes, the successive acidification of the cytosol did not appreciably alter EGFP and citrine fluorescence emission spectra down to pH values of 4.8 (Fig. 3a) and 5.2 (Fig. 3b), respectively. However, while their shape proved robust against pH changes, their intensity rapidly declined upon acidification (Fig. 2c, d). Upon return to pH 7.3, the shape of the spectrum was recovered, even after having attained pH 4.3. The incomplete recovery of EGFP intensity beyond pH 5.0 (data not shown) is consistent with Verkman's earlier work and, probably due to a decreased solubility, can be taken as an internal control that the cytoplasm indeed had reached pH values below 5 (Kneen et al. 1998). We conclude that the acidic vesicle lumen does not appreciably shift the fluorophore spectral signature compared to the cytoplasmic controls but, due to the fainter signal at low pH, increases the impact of noise on the accuracy of the measured spectra (see Discussion).

Despite their insensitivity to pH effects, the recorded pure spectra displayed some variability from cell to cell and even from one organelle to another (see superimposed grey traces on Fig. 2b, right panel). The accuracy of the reference and unmixed spectra and their degree of variability determine the accuracy of the fluorophore abundance estimate. This effect is illustrated when unmixing spectra taken in control situations where only one fluorophore was present. In this situation, only the respective fluorophore truly present should be detected while the proportion of false positives should be close to zero. We plot on Fig. 4a the pure spectral abundance vectors $\langle \hat{\alpha}(i) \rangle_l = (\alpha_{EGFP}, \alpha_{citrine}, \alpha_{AF})$ in a space spanned by the pure EGFP, citrine and AF unit vectors. As expected, the values of $\langle \hat{\alpha}(i) \rangle_l$ are close to the orthogonal unit vectors for all three fluorophores (see Table 1 for the mean $\pm$ SD). A score between 0 and 1 rates the estimated fractional abundance of each fluorophore, 1 equalling a perfect match. For greater clarity, we show the 2D projection of $\hat{\alpha}(i)$ onto the plane $\mathbf{1}^T \cdot \hat{\alpha} = 1$ (shaded on panel a, Fig. 4b) instead of a pseudo-3D plot. On the triangular plot (its parameterisation in the new co-ordinates X and Y is given in Appendix) pure spectral vectors are expected to populate the corners. As anticipated from the larger spectral variability of AF, we observe a larger dispersion of the reconstituted component of $\hat{\alpha}(i)$ for AF (1.000 ± 0.016) than for EGFP (1.001 ± 0.002) and citrine (0.999 ± 0.002). Thus, even for AF, unit vectors are recovered with less than 2% relative error and the estimates of EGFP and citrine in pure AF cells are equal to zero (see Table 1). Our data hence

Table 1 Reconstituted pure fluorophore abundances

	EGFP	Citrine	AF
$\langle \hat{\alpha}(\text{EGFP}) \rangle_l$	1.001 ± 0.002	0.000 ± 0.004	-0.001 ± 0.002
$\langle \hat{\alpha}(\text{citrine}) \rangle_l$	0.002 ± 0.002	0.999 ± 0.002	0.000 ± 0.002
$\langle \hat{\alpha}(\text{AF}) \rangle_l$	0.000 ± 0.026	0.000 ± 0.026	1.000 ± 0.016

confirm the previous observation that despite the presence of image noise and spectral heterogeneity a few spectral detection bands suffice to correctly classify spectrally overlapping fluorophores (Neher and Neher 2004a).

In the following, we therefore use the reconstituted pure EGFP and citrine vector bundles to define zones of fluorophore presence for testing if a spectral vector belongs to $\{\hat{\alpha}'\}_{\text{EGFP}}$ or $\{\hat{\alpha}'\}_{\text{citrine}}$, respectively.

The main interest of spectral single-vesicle imaging and linear unmixing is its potential to detect FP expression in the presence of a spectrally overlapping and spatially varying autofluorescence. We consequently investigated in sb2-EGFP or sb2-citrine-transfected astrocytes if SILU recognised fluorescent protein expression on single secretory vesicles. Spectral vectors $\mathbf{w}(i)$ of FP expressing organelles differed from AF ROIs when testing for outliers against the pure AF vector bundle $\{\mathbf{w}(\text{AF})\}$ (Fig. 5a, left, cf. Eq. 7). To compare organelles across cells with different AF levels, we re-normalised $\hat{\alpha}' = (\alpha_{\text{EGFP}}, \alpha_{\text{citrine}})/(1 - \alpha_{\text{AF}})$ and plotted α'_{EGFP} versus α'_{citrine} (middle panel). Testing if $\hat{\alpha}'(i)$ was an outlier relative to the previously obtained (and re-normalised) pure spectral vector bundles $\{\hat{\alpha}'_{\text{EGFP}}\}$ and $\{\hat{\alpha}'_{\text{citrine}}\}$ defined detection thresholds $\hat{\alpha}'_{\text{EGFP}} = (0.965 \pm 0.034)$ for EGFP and $\hat{\alpha}'_{\text{citrine}} = (0.976 \pm 0.023)$ for citrine, respectively, meaning that an $\hat{\alpha}'$ located in the rectangular region bounded by dotted lines designates the presence of both EGFP and citrine. Indeed, in control cells that were contransfected with EGFP and citrine (Fig. 5b), all 25 analysed spots fell within the bounded region. Their average was $\langle \hat{\alpha}' \rangle = (0.331 \pm 0.008, 0.669 \pm 0.008)$.

We next unmixed 25 fluorescent spots in cells that were either transfected with sb2-EGFP (green) or sb2-citrine (red, Fig. 5a, middle panel). On the rightmost panel we show for comparison the previously measured pure abundances for the cytoplasmic expression of the same FPs, in re-normalised co-ordinates $\{\hat{\alpha}'_{\text{EGFP}}\}$ and $\{\hat{\alpha}'_{\text{citrine}}\}$. Organelle spectral abundance vectors $\hat{\alpha}'(i)$ of pure EGFP or citrine-expressing vesicles displayed a wider distribution than the corresponding cytoplasmic controls and have larger confidence intervals than their cytoplasmic counterparts. For the same gain and integration time, single fluorescent organelles images are dimmer (and hence more noisy) and thus display more spectral variability than resolution-limited homogeneously fluorescent sample voxels (see below).

Perhaps SILU-based fluorophore abundance estimates are biased by sampling off-focus fluorescence above and below the studied (sub-resolution) organelle. An average vesicle measures 30–300 nm in diameter and

is much smaller than the axial extent of the experimental point-spread function (Fig. 1c). Also, fluorophores may not exclusively be localised on secretory organelles. For example, although predominantly targeted to secretory vesicles, sb2 is only partially recaptured after fusion and partly diffuses in the plasma membrane (D. Perrais, personal communication). Corroborating this observation, sb2-citrine-expressing astrocytes (Fig. 1a) displayed a luminous hazy background that was absent in EGFP-sialine-expressing cells (panel b). To ascertain a vesicular localisation of the FP chimera and to exclude false positives that could result from membranous or cytoplasmically expressed fluorophores above focus, we introduced a spatial contrast parameter based on reconstituted fluorophore abundance maps. The participation of pure spectra to each pixel (x, y) was calculated by multiplying $\hat{\alpha} * (x, y)$ componentwise with the scaling factor $\sum_{k=1}^{N} w_k (x, y)$. Spatial contrast was then defined as the amplitude of the central $\hat{\alpha}(i)$ relative to 16 control regions in the periphery of spot i (Fig. 5b). On near-diffraction-limited images, a vesicular or lysosomal fluorophore localisation should be detectable as a central outlier. In contrast, a diffuse cytoplasmic or membranous localisation should produce a flat contrast. We validated our approach by first studying defined control transfections. Figure 5b shows a pseudocolour spatial abundance map for cytoplasmically co-expressed EGFP and citrine. As expected, the volumetric (false) co-localisation of cytoplasmically EGFP and citrine produces a flat contrast, indicating that the estimated abundance in the central 3×3-pixel ROI was not statistically different from the surrounding 16 ROIs (Student's test, see below). In contrast, EGFP- and citrine positive were reliably detected as outliers (panels c and d). We therefore classified an organelle as co-expressing EGFP and citrine, if (1) both EGFP and citrine were detected in the central ROI and (2) the spatial contrast for both EGFP and citrine showed a central outlier. The results of the statistical test are quantified in the right-
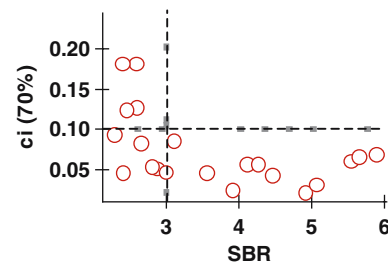

Fig. 6 Evolution of the confidence interval (ci) for estimating α_{EGFP} with increasing signal-to-background ratio (SBR). Each *spot* represents an unmixed organelle in a sb2-EGFP/sb2-citrine co-transfected astrocyte. Signal was measured as the average intensity in an Airy disk-sized 3×3-pixel region centred on the spot. Background intensities were measured in nearby cell-free regions with the same gain and exposure time. The accuracy of the estimation of α_{EGFP} increases with higher signals. Estimates of α_{EGFP} with a precision better than 10% (*dashed line*) require a signal three times above background

most column of Fig. 5 by plotting, for each analysed ROI, a barbell the endpoints of which indicate the contrast in the EGFP and citrine-reconstituted images, respectively. ROIs were dubbed FP labelled when their contrast exceeded Student's $t_{95\%} > 1.76$. We used red and green symbols to designate citrine- and EGFP-positive organelles, respectively. Black symbols indicate diffuse expression, yellow shows specific co-localisation on the studied organelle. The same colour code was then assigned to the spots on 2D abundance maps. A colour version of Fig. 5 is available online

Both the detection of protein presence on the organelle and the estimated degree of co-localisation depend on the desired confidence level (Table 2). We take the example of control cells that were transfected with the fusion protein encoding sb2-EGFP only. If EGFP shall be detected with 99% certainty, 72% of the fluorescent organelles expressing another fluorophore than AF alone are recognised EGFP-positive. No organelle is classified as citrine-positive, but 28% of the fluorescent organelles are discarded, because no decision can be reached with 99% confidence. If, however, the confidence for EGFP detection is lowered to 95%, the fraction of non-classified organelles drops to 4%, and 96% organelles are recognised EGFP-positive. When tolerating 10% error for organelle classification, 92% organelles are classified EGFP-positive. This apparent drop is explained by the observation that now 8% are (falsely) dubbed citrine-positive, and none remains unclassified. Hence, in practice, a compromise must be reached between detecting a sufficiently large fraction of fluorescent organelles to constitute a representative sample and accepting a false classification. In our hands, 95% confidence ($t_{95\%} = 1.76$ for *Student's*-distribution, see the dotted line on the rightmost panel of Fig. 5b–d) proved a good choice for detecting fluorescently labelled secretory organelles in cell culture.

Finally, we illustrate the performance of our technique for detecting co-localisation by co-expressing sb2-EGFP and sb2-citrine together (Fig. 5c). After the successful elimination of only-autofluorescent ROIs SILU finds, with 95% confidence, 40% organelles EGFP-positive, 8% citrine-positive and 52% expressing both fluorescent proteins. This observation is in stark contrast to previous controls in which a single fluorescent protein was expressed and virtually no (false) co-localisation was detected (Table 2). The surprisingly low fraction (8%) of citrine-(only) positive organelles compared to the fivefold higher fraction of EGFP-expressing secretory vesicles is most likely due to the faint luminosity of citrine compared to EGFP (see below and Fig. 3).

When instead co-expressing the lysosomal transporter sialine tagged with EGFP together with the vesicle marker sb2-citrine (Fig. 5d) we found a substantially lower 28% overlap; 64% of the studied spots expressed EGFP only, and almost no citrine was detected alone, probably indicating the degradation of membraneously overexpressed sb2 in lysosomal compartments. This result is also plausible in view of the observation that lysosomes largely outnumber secretory vesicles in cultured astrocytes (Nadrigny and Oheim, unpublished data).

Discussion

Multi- and hyperspectral imaging are utilised in air- and spaceborne remote sensing of Earth topography, environmental monitoring, mapping and management of water or agricultural resources to detect the presence in mixed pixels of several endmembers, the fractional surface coverage of which is often much lower than the monitored area represented in one image pixel. Microscopic fluorescence imaging differs from these applications in that it provides diffraction-limited images on which point objects are spread over several adjacent image pixels, which are no longer independent. In this study, we took advantage of their statistic interdependence to extract noise-reduced organelle spectra and to unmix resolution-limited single-vesicle images. We also derived the m-dimensional confidence interval of SILU-based fluorophore abundance estimates $\hat{\alpha}(i)$.

Heterogeneous vesicle populations have previously been studied after immunocytochemical labelling with specific antibodies by confocal imaging (Parpura et al. 1995), deconvolution-assisted fluorescence microscopy (Anlauf and Derouiche 2005) or immuno-electron microscopy (Bezzi et al. 2004) in fixed preparations. Alternatively, local ultrasound pulses generate semi-intact "unroofed" cells. Due to their flatness, these "plasma membrane lawns" permit the visualisation of single membrane-attached vesicles (Lang 2003; Wiegand et al. 2002). Sub-cellular fractionation and subsequent gradient-density centrifugation (Calegari et al. 1999; Papini et al. 1995) or vesicle isolation on immunobeads (Chilcote et al. 1995) are cell-free alternatives for classifying vesicles.

Clearly, a better understanding of the dynamic mechanisms and the regulation of the parallel secretory pathways that coexist both in non (electrically) excitable cells (Chieregatti and Medolesi 2005) like astroglia (Coco et al. 2003; Mothet et al. 2005) but also in neu-

Table 2 Profiling protein expression on single vesicles

$n = 25$ each	Classified EGFP (%)	Classified citrine (%)	Co-localised (%)
sb2-EGFP	72, *96*, 92	0, *0*, 0	0, *0*, 8
sb2-citrine	0, *0*, 0	40, *68*, 88	0, *4*, 4
sb2-EGFP + sb2-citrine	56, *42*, 32	8, *8*, 4	32, *52*, 64
EGFP-sialine + sb2-citrine	64, *64*, 56	8, *0*, 0	4, *28*, 36

Differences to 100% are due to spots for which decision was impossible. We counted hits for detecting fluorescent proteins with 99, *95*, and 90% confidence, respectively. Lower expression detection thresholds engender a larger probability of detecting false co-localisation (also)

rones and that co-release different transmitters requires time-lapse imaging of intact cells rather than fractionalised or semi-intact preparations.

The imaging and tracking over time of distinct sub-cellular single vesicular compartments labelled with specific fluorescent fusion proteins has become possible (Steyer et al. 1997; Oheim et al. 1998) with EF excitation of fluorescence (see, e.g. Schneckenburger 2002; Axelrod 2003 for recent reviews). However, the multiplexed detection of spectral variants of FP requires spectrally separated probes and negligible autofluorescence. Although monomeric red fluorescent jellyfish and coral proteins are increasingly becoming available in addition to yellow and green fluorescent fusion proteins for double or triple labelling experiments (Verkhusha and Lukyanov 2004), we found that the transient expression of the vesicle-associated membrane protein VAMP-2 (synaptobrevin-2, sb2) tagged with red fluorescent proteins (DsRed, mDsRed, hcRed) failed to produce a homogenous cytoplasmic expression in controls (data not shown). Similarly, transgenic mice expressing red coral proteins produced fluorescent precipitates that precluded a detailed morphological analysis (Hirrlinger et al. 2005).

In turn, the available cyan, green, yellow and orange FPs display a strong cross-excitation and emission spectral overlap that precludes their separation using dual or triple emission band-pass filters. Importantly, even with non-precipitating red fluorescent labels, the observed spectrally broad autofluorescence (AF) would still obscure FP expression and preclude an unambiguous identification of labelled organelles. Therefore, dual band-pass recordings do not provide a suitable way to reliably quantify co-localisation in the present experimental scenario.

In the present study, we demonstrate that SILU is a powerful tool to quantitate the expression and co-localisation of spectrally overlapping proteins in live cells with diffraction-limited spatial resolution. While this observation hardly comes as a surprise, our study provides the theoretical framework for quantitative SILU of single diffraction-limited point objects and derives the precision that can be attained. Over splitting the intensity into several multiplexed detection bands, we opted for the sequential acquisition of spectrally overlapping bands (Fig. 2). While this choice reduces the time resolution in proportion to the number of detection bands it optimises the signal-to-noise ratio and precision of the technique (see below). In many experiments, however, the organelle spectra will be constant on the time scale of the image acquisition, because the underlying biological processes (protein expression, sub-unit composition, etc.) are relatively slow. In these applications, it is sufficient to take a spectral "snapshot" at the beginning of the time-lapse acquisition and then to track the classified organelles with higher temporal resolution on a single-wavelength movie. The same argument holds for experiments with only slowly varying spectra: for example, Duncan et al. (2003) took advantage of the

time-dependent spectral shift of a fluorescent timer protein to demonstrate that individual chromaffin granules are segregated functionally and spatially according to age. Likewise, photoswitchable GFP variants (Chudakov et al. 2004) display highly overlapping fluorescence before and after photoactivation. Semiconductor nanocrystals (quantum dots) undergo a gradual blue shift in their emission spectrum due to surface oxidation in response to prolonged illumination (Grecco et al. 2004), which will be captured on sequential spectral snapshots, interlaced with faster time-lapse imaging. We note that some applications that measure dynamic changes in overlapping spectra like spectral FRET detection (Ishii et al. 1999) might benefit from projecting different images side by side on the same CCD camera (Mattheyses et al. 2004) or simultaneously on several detectors so as to increase the time resolution at the expense of SILU precision.

We deliberately chose a combination of EF and epifluorescence excitation, to identify individual near-membrane candidate vesicles for unmixing and epifluorescence for acquiring spectral images cubes. Epifluorescence integrates over a micrometre axial volume (Fig. 1c), thereby rendering SILU estimates insensitive against small axial organelle movements and defocus. However, the use of epifluorescence instead of EF excitation to acquire spectra engenders a loss of contrast and a decrease in the axial resolution. In as much as we unmixed only organelles that appeared both on EF and epifluorescence images and accounted for out-of-focus blur by statistically testing for organelle presence (centre vs. surround), the *effective* resolution is not affected. However, epifluorescence imaging will preclude reasonable SILU estimates in situations where the organelle density is high. To be sure the recorded spectrum of a spot was not contaminated by nearby out-of-focus organelles, we selected (and rejected) ROIs in relation to the experimental PSF (Fig. 1c), which defines an observation volume in which only one organelle should be present. The lateral PSF of the microscope is described by a Bessel function with the second zero located at 625 nm (3.3 pixels) from its centre. This distance corresponds to 99.6% attenuation and defines a ring around the 3×3 pixels ROI (i.e. an overall diameter $d = 9$ pixels) in which no other organelle must be present. In axial direction, the second zero z_2 is located at 3.4 µm from the focus plane. Hence, the studied organelle must be alone in a cigar-shaped volume of $V = \pi \ d^2 / 4z_2 = 8.3 \ \mu m^3$. With roughly 0.01 organelles/µm^3 in cultured astrocytes we expect $n = \rho \ V \sim 0.08$ organelles in this volume element. So there is a very low probability that a second organelle would be present in the readout volume.

One important finding of our experiments is that *ceterum paribus* citrine expression is less easily recognised than EGFP labelling (Table 2). Is this difficulty related to the dimmer citrine fluorescence, its larger pH sensitivity (Heikal et al. 2000), or the larger similarity between citrine and AF spectra than between EGFP and

AF? We can indirectly exclude the last possibility by noting that a variable amount of autofluorescence does not influence the precision of our α_{citrine} or α_{EGFP} estimates (Supplementary Fig. 1). Second, SILU does not detect more AF in pure citrine than in pure EGFP and also does not falsely recognise more citrine than EGFP in non-labelled (only AF) cells (Table 1). Furthermore, our spectral measurements at different pHs demonstrate that the EGFP spectrum does not appreciably change down to pH 4.8 so that the reference spectrum recorded in the cytoplasm is a good template for that expected in secretory organelles. Indeed, we find 96% sb2-EGFP-positive organelles ($N = 25$) when unmixing an EGFP-sb2-transfected cells. In contrary, the citrine spectrum begins to change at pH 5.2 so that there could be a slight difference between the cytoplasmic reference spectrum and the spectrum in organelles. We detect only 68% of citrine-sb2-positive organelles in citrine-sb2-transfected cells ($N = 25$). However, the same results were obtained when we unmixed these organelles with the citrine spectra acquired at pH 5.2 instead, and bigger errors and same or lower detection were obtained with the reference spectra recorded at even lower pH (5.0 or 4.8). Thus, we conclude that as for EGFP, the vesicular citrine spectrum is not appreciably different from its cytoplasmic reference and that it can be used for unmixing citrine expressed in mildly acidic organelles. Rather, citrine-labelled organelles are dimmer than EGFP-labelled ones. This is not an indirect pH effect, because both EGFP and citrine intensities show a similar pH dependence (Fig. 3c, d). On average, spots in sb2-EGFP-transfected cells displayed a centre versus surround contrast ratio of 0.67 ± 0.30 compared to 0.32 ± 0.14 for citrine ($N = 25$, $P < 0.0001$). Thus, the slight variation in the spectral shape of citrine at pH lower than 5.2 at both dimmer ends may be partially due to its lower brightness and hence larger relative contribution of image noise (cf. the size of the normalised SD in Fig. 3c, d). Indeed, low-intensity spots generally have a spectrum slightly different from the brighter ones (data not shown). Actually, this difference in brightness between EGFP and citrine was predictable because 458-nm excitation is more efficient for the former. Longer-wavelength excitation offers little room for improvement as the transmission light and also the noise in the first 510 nm emission channel would increase at the same time.

Thus, the lower probability to detect citrine-labelled organelles is rather attributable to the lower brightness of citrine compared to EGFP than to different responses to acidic pH. Our results illustrate that a sufficiently high image contrast is required to successfully unmix labelled organelles. Finally, which signal-to-background ratio (SBR) is required to attain a given SILU confidence level? Figure 6 plots, for a representative sample of fluorescent spots from a sb2-EGFP/sb-citrine co-transfected astrocyte, the 70% confidence interval of the estimated fractional abundance of EGFP, α'_{EGFP}, as a function of the spot's SBR ($n = 21$). Background intensities were measured in nearby cell-free regions with the same gain and exposure time. As expected, a higher SBR favours the accurate determination of α'_{EGFP}. To obtain estimates of α'_{EGFP} with a precision $\Delta \alpha'_{\text{EGFP}}/\alpha'_{\text{EGFP}}$ better than 10% (dashed line) requires an average vesicle signal exceeding three times the image background. For example, the analysed spots in astrocytes that were transfected with sb2-EGFP or sb2-citrine, respectively, had an average SBR of 11.5 ± 4.7 and 9.3 ± 5.2 and hence allowed good precision estimates (Fig. 6).

In conclusion our results demonstrate that SILU of spatially and spectrally correlated Airy disk-sized regions provides robust estimates of protein expression and co-localisation on individual exocytic and non-secretory compartments (Chieregatti and Medolesi 2005) in live cells. We expect our technique to be influential in a large variety of cell and neurobiological applications where conventional dual or triple colour measurements fail to produce reliable co-localisation data.

Appendix

Parameterisation of the 2D projection of the 3D fluorophore abundance vector onto the plane $\mathbf{1}^{\text{T}} \cdot \hat{\alpha} = 1$.

For the tertiary mixture of AF, EGFP, citrine, the estimated fluorophore abundance $\hat{\alpha}(i)$ is a vector in 3D space, spanned by the EGFP, citrine and AF unit vectors, respectively (Table 1). However, its pseudo-3D representation does not lend itself to a clear graphic representation of an appreciable number of unmixed spots. Thus, for greater clarity, we plot on Fig. 4b its 2D projection onto the plane $\mathbf{1}^{\text{T}} \cdot \hat{\alpha} = 1$ (shaded on panel a), parameterised by X and Y,

$$X = \sin\varphi \sqrt{\alpha_{\text{EGFP}}^2 + \alpha_{\text{citrine}}^2},$$
$$Y = \cos\left[\arctan\left(2/\sqrt{2}\right) - \arctan\left(\alpha_{\text{AF}}/B\right)\right] \cdot \sqrt{\alpha_{\text{AF}}^2 + B^2},$$

$$(10)$$

where

$$B = \left| \frac{\sqrt{2}}{2} - \cos\varphi \cdot \sqrt{\alpha_{\text{EGFP}}^2 + \alpha_{\text{citrine}}^2} \right|$$

$$\varphi = \begin{cases} \frac{\pi}{4} - \left[\arctan\left(\alpha_{\text{EGFP}}/\alpha_{\text{citrine}}\right)\right] & \text{for } \alpha_{\text{citrine}} > 0 \\ -\frac{3\pi}{4} - \left[\arctan\left(\alpha_{\text{EGFP}}/\alpha_{\text{citrine}}\right)\right] & \text{else} \end{cases} \quad . \quad (11)$$

Here, ϕ denotes the angle (positive or negative angle) between the vectors (α_{EGFP}, $\alpha_{citrine}$, 0) and (1, 1, 0).

References

Anlauf E, Derouiche A (2005) Astrocytic exocytosis vesicles and glutamate: a high-resolution immunofluorescence study. Glia 49(1):96–106

Bezzi P, Gundersen V, Galbete JL, Seifert G, Steinhäuser C, Pilati E, Volterra A (2004) Astrocytes contain a vesicular compartment that is competent for regulated exocytosis. Nat Neurosci 7:613–620

Bosdogianni P, Petrou M (1997) Mixed pixel classification with robust statistics. IEEE Trans Geosci Remote Sens 35(3):551–559

Bosdogianni P, Petrou M, Kittler J (1997) Mixture models with higher order moments. IEEE Trans Geosci Remote Sens 35(2):341–353

Calegari F, Coco S, Tarverna E, Bassetti M, Verderio C, Corradi N, Matteoli M, Rosa P (1999) A regulated secretory pathway in cultured hippocampal astrocytes. J Biol Chem 274:22539–22547

Chang CI (2003) Hyperspectral imaging: techniques for spectral detection and classification. Kluwer Plenum, New York

Chieregatti E, Medolesi J (2005) Regulated exocytosis: new organelles for non-secretory purposes. Nature reviews. Mol Cell Biol 6:181–187

Chilcote T, Galli T, Mundigl O, Edelmann L, McPherson P, Takei K, De Camilli P (1995) Cellubrevin and synaptobrevins: similar subcellular localization and biochemical properties in PC12 cells. J Cell Biol 129:219–231

Chudakov DM, Verkhusha VV, Staroverov DB, Souslova EA, Lukyanov S, Lukyanov KA (2004) Photoswitchable cyan fluorescent protein for protein tracking. Nat Biotechnol 22:1435–1439

Coco S, Calegari F, Pravettoni E, Pozzi D, Taverna E, Rosa P, Matteoli M, Verderio C (2003) Storage and release of ATP from astrocytes in culture. J Biol Chem 278:1354–1362

Demuro A, Parker I (2004) Imaging the activity and localization of single voltage-gated Ca^{2+} channels by total internal reflection fluorescence microscopy. Biophys J 86:3250–3259

Dickinson ME, Bearman G, Tille S, Lansford R, Fraser SE (2001) Multi-spectral imaging and linear unmixing add a whole new dimension to laser scanning fluorescence microscopy. BioTechniques 31:1272–1278

Duncan RR, Greaves J, Wiegand UK, Matskevich I, Bodammer G, Apps DK, Shipston MJ, Chow RH (2003) Functional and spatial segregation of secretory vesicle pools according to vesicle age. Nature 422:176–180

Ecker RC, de Martin R, Steiner GE, Schmid JA (2004) Application of spectral imaging microscopy in cytomics and fluorescence resonance energy transfer (FRET) analysis. Cytometry (Pt A) 59A:172–181

Ellenberg J, Lippincott-Schwartz J (1999) Dual-colour imaging with GFP variants. Trends Cell Biol 9:52–56

Garini Y, Gil A, Bar-Am I, Cabib D, Katzir N (1999) Signal to noise analysis of multiple color fluorescence imaging microscopy. Cytometry 35:214–226

Grecco HE, Lidke KA, Heintzmann R, Lidke DS, Spagnuolo C, Martinez OE, Jares-Erijman EA, Jovin TM (2004) Ensemble and single particle photophysical properties (two-photon excitation, anisotropy, FRET, lifetime, spectral conversion) of commercial quantum dots in solution and in live cells. Microsc Res Tech 65:169–179

Griesbeck O, Baird GS, Campbell RE, Zacharias DA, Tsien RY (2001) Reducing the environmental sensitivity of yellow fluorescent protein. J Biol Chem 276:29188–29194

Gu Y, Di WL, Kelsell DP, Zicha D (2004) Quantitative fluorescence resonance energy transfer (FRET) measurement with acceptor photobleaching and spectral unmixing. J Microsc 215:162–173

Heikal AA, Hess ST, Baird GS, Tsien RY, Webb WW (2000) Molecular spectroscopy and dynamics of intrinsically fluorescent proteins: coral red (dsRed) and yellow (citrine). Proc Natl Acad Sci USA 24(97):11996–12001

Hiraoka Y, Shimi T, Haraguchi T (2002) Multispectral imaging fluorescence microscopy for living cells. Cell Struct Funct 27:367–374

Hirrlinger PG, Scheller A, Braun C, Quintela-Schneider M, Fuss B, Hirrlinger J, Kirchhoff F (2005) Expression of red coral fluorescent proteins in the central nervous system of transgenic mice. Mol Cell Neurosci 30:291–303

Ishii Y, Yoshida T, Funatsu T, Wazawa T, Yanagida T (1999) Fluorescence resonance energy transfer between single fluorophores attached to a coiled-coil protein in aqueous solution. Chem Phys 247:163–173

Kneen M, Farinas J, Li Y, Verkman AS (1998) Green fluorescent protein as a noninvasive intracellular pH indicator. Biophys J 74:1591–1599

Lang T (2003) Imaging SNAREs at work in 'unroofed' cells—approaches that may be of general interest for functional studies on membrane proteins. Biochem Soc Trans 31:861–864

Lansford R, Bearman G, Fraser SE (2001) Resolution of multiple green fluorescent protein color variants and dyes using two-photon microscopy and imaging spectroscopy. J Biomed Opt 6:311–318

Mattheyses AL, Hoppe AD, Axelrod D (2004) Polarized fluorescence resonance energy transfer microscopy. Biophys J 87(4):2787–2797

Michalet X, Lacoste TD, Pinaud F, Chemla DS, Alivisatos AP, Weiss S (2001) Ultrahigh Resolution multicolor colocalization of single fluorescent nanocrystals. Nanoparticles and nano-structured surfaces: novel reporters with biological applications. Proc SPIE 4258

Morin P, Sagne C, Gasnier B (2004) Functional characterization of wild-type and mutant human sialin. EMBO J 23:4560–4570

Mothet J-P, Pollegioni L, Ouanounou G, Martineau M, Fossier P, Baux G (2005) Glutamate receptor activation triggers a calcium-dependent and SNARE protein-dependent release of the gliotransmitter D-serine. PNAS 102:5606–5611

Neher F, Neher E (2004a) Optimizing imaging parameters for the separation of multiple labels in a fluorescence image. J Microsc 213:46–62

Neher RA, Neher E (2004b) Applying spectral fingerprinting to the analysis of FRET images. Microsc Res Tech 64:185–195

Nielsen AA (2001) Spectral mixture analysis: linear and semiparametric full and iterated partial unmixing in multi- and hyperspectral image data. Int J Comp Vis 42:17–37

Oheim M, Loerke D, Stühmer W, Chow RH (1998) The last few milliseconds in the life of a secretory granule. Docking, dynamics and fusion visualized by total internal reflection fluorescence microscopy (TIRFM). Eur Biophys J 27:83–98

Oshiro M, Moomaw B (2003) Cooled vs. intensified vs. electron bombardment CCD cameras—applications and relative advantages. Methods Cell Biol 72:133–156

Papini E, Rossetto O, Cutler DF (1995) Vesicle-associated membrane protein (VAMP)/synaptobrevin-2 is associated with large dense core secretory granules in PC12 neuroendocrine cells. J Biol Chem 270:1332–1336

Parpura V, Fang Y, Basarsky T, Jahn R, Haydon PG (1995) Expression of synaptobrevin II, cellubrevin and syntaxin but not SNAP-25 in cultured astrocytes. FEBS Lett 337:489–492

Rouach N, Segal M, Koulakoff A, Giaume C, Avignone E (2003) Carbenoxolone blockade of neuronal network activity in culture is not mediated by an action on gap junctions. J Physiol 553:729–745

Schapper F, Gonçalves JT, Oheim M (2003) Fluorescence imaging with two-photon evanescent-wave excitation. Eur Biophys J 32:635–645

Schipper HM, Small L, Wang X, Brawer JR (2002) Role of porphyrin sequestration in the biogenesis of iron-laden astrocytic inclusions in primary culture. Dev Neurosci 24:169–176

Schneckenburger H (2002) Total internal reflection fluorescence microscopy: technical innovations and novel applications. Curr Opin Biotechnol 16:13–18

Schultz RA, Nielsen T, Zavaleta JR, Ruch R, Wyatt R, Garner HR (2001) Hyperspectral imaging: a novel approach for microscopic analysis. Cytometry 43:239–247

Shirakawa H, Miyazaki S (2004) Blind spectral decomposition of single-cell fluorescence by parallel factor analysis. Biophys J 86:1739–1752

Stephens DJ, Lin-Marq N, Pagano A, Pepperkok R, Paccaud JP (2000) COPI-coated ER-to-Golgi transport complexes segregate from COPII in close proximity to ER exit sites. J Cell Sci 113:2177–2185

Steyer JA, Horstmann H, Almers W (1997) Transport, docking and exocytosis of single secretory granules in live chromaffin cells. Nature 388:474–478

Tsurui H, Nishimura H, Hattori S, Hirose S, Okumura K, Shirai T (2000) Seven-color fluorescence imaging of tissue samples based on Fourier spectroscopy and singular value decomposition. J Histochem Cytochem 48:653–662

Verkhusha VV, Lukyanov KA (2004) The molecular properties and applications of Anthozoa fluorescent proteins and chromoproteins. Nat Biotechnol 22:289–296

Wiegand UK, Don-Wauchope A, Matskevich I, Duncan RR, Greaves J, Shipston MJ, Apps DK, Chow RH (2002) Exocytosis studies in a chromaffin cell-free system: imaging of single-vesicle exocytosis in a chromaffin cell-free system using total internal reflection fluorescence microscopy. Ann NY Acad Sci 971:257–261

Wojcik SM, Rhee JS, Herzog E, Sigler A, Jahn R, Takamori S, Brose N, Rosenmund C (2004) An essential role for vesicular glutamate transporter 1 (VGLUT1) in postnatal development and control of quantal size. Proc Acad Sci USA 101:7158–7163

Zimmermann T (2005) Spectral imaging and linear unmixing in light microscopy. Adv Biochem Eng Biotechnol 95:245–265

Zimmermann T, Rietdorf J, Pepperkok R (2003) Spectral imaging and its application in live cell microscopy. FEBS Lett 546:87–92